



In situ synthesis of nanocomposite materials based on modified-mesoporous silica MCM-41 and methyl methacrylate for copper (II) adsorption from aqueous solution

Gholamhossein Mohammadnezhad¹ · Parisa Moshiri¹ · Mohammad Dinari¹ · Frank Steiniger²

Received: 25 July 2018 / Accepted: 2 February 2019 / Published online: 9 February 2019
© Iranian Chemical Society 2019

Abstract

In this study, amine-modified MCM-41/poly(methyl methacrylate) nanocomposites (m-MCM-41/PMMA NCs) were fabricated through in situ polymerization method and ultrasonic irradiation technique. The as-prepared nanocomposites were utilized for adsorption of Cu^{2+} ions from aqueous media. Physico-chemical properties of m-MCM-41/PMMA NCs were studied by thermogravimetric analysis (TGA), transmission and scanning electron microscopes (TEM and SEM), small angle X-ray scattering (SAXS), and Fourier transform infrared (FT-IR) spectroscopy. Based on analysis data, 2 wt% NC was selected for adsorption studies and the pH effect, contact time, and initial concentration of metal ions was investigated. The adsorption mechanism and kinetics were evaluated using three kinetic models namely pseudo-second-order, Elovich, and intraparticle diffusion. In addition, the adsorptive performance of the selected NC was investigated by two common isotherm models namely Langmuir and Freundlich. Kinetics and isotherm equilibrium data showed acceptable fitting with the pseudo-second-order and Langmuir model, respectively. The maximum value of adsorption capacity toward copper(II) ions was found to be 41.5 mg g^{-1} (pH = 4, adsorbent dose 10 mg, temperature $25 \text{ }^\circ\text{C}$, stirring speed 180 rpm, and time 140 min).

Keywords Nanocomposites · Mesoporous · Poly(methyl methacrylate) · Copper (II) removal · Adsorption isotherms

Introduction

Heavy metal-induced pollution is rightly considered a serious threat to human health as well as the environment [1, 2]. Various techniques such as reverse osmosis, ion exchange, membrane filtration, chemical chelating precipitation, electrochemical remediation, coagulation, and adsorption have all proved to be effective in their removal [3–6]. Out of these techniques, the adsorption strategy is a clear standout candidate and has been regarded as the most popular, economical, and efficient strategy stemming from its high efficiency and simplicity of use without making any accompanying operational problems. In addition, it is considered as a beneficial technique because of its flexible design, reversibility, high

efficiency, good performance, and eco-friendliness even in large-scale manufacturing [6–8]. This method typically relies on the suitability of the applied adsorbents and nanocomposites belong to one of the most effective classes of adsorbents.

Nanocomposites are a new generation of advanced compounds whose development was borne out of the desire to monitor and control interfacial interaction at both micro- and nanoscale [9–11]. The synthesis of the nanocomposite materials is typically achieved via co-assembling of organic and inorganic precursors (at least one of the precursors should have a nano dimension) [12, 13]. In this way, the characteristics and functions of these composite materials would be completely different from the individual components. To gain the best advantages of organic–inorganic nanocomposites, the sizes and topologies of individual domains as well as their interfaces should be optimized. It is likewise crucial that a homogeneous distribution of nanoparticles is achieved, to enhance the properties of obtained nanocomposites [14–21]. In addition, the processability of the materials is vital to unlocking the full potential of their technological use. In this regard, polymers are considered as

✉ Gholamhossein Mohammadnezhad
mohammadnezhad@cc.iut.ac.ir; g_m1358@yahoo.com

¹ Department of Chemistry, Isfahan University of Technology, Isfahan 84156-83111, Islamic Republic of Iran

² Center for Electron Microscopy, Jena University Hospital, Ziegelmühlenweg 1, 07743 Jena, Germany

an essential part of advanced materials, which ultimately resulted in the discovery of a new class of hybrid materials known as polymer nanocomposites.

Recently, several synthetic approaches have been established for better optimization of the properties of the nanostructure materials, such as their shape and size. Ultrasonic irradiation is one of the important synthetic methods and it has the advantage of being eco-friendly, simple, and flexible. However, in comparison with other techniques, it is not so affordable. Nonetheless, among other energy sources, ultrasonic irradiation provides exceptional reaction conditions including remarkably short reaction time, high temperature, and pressure. While on a general note, ultrasound energy does not interact with substances at a molecular level, it is nevertheless useful chemically. This is even more so when intense ultrasound irradiation is used, as this leads to acoustic cavitation, i.e., formation, growth, and a burst of bubbles gas in solutions. Most high-intensity ultrasound devices run above 20 kHz while some of them are suitable for low MHz ranges. This technique was also used for facile preparation of a wide variety of nanocomposites, leading to a constructive influence on the different factors. It has been observed to result in an increased active surface, enhanced distribution of nanofillers as well as deagglomeration of both polymer and nanofiller. Ultimately, for the desired nanocomposites to be prepared, ultrasonic irradiation was applied to increase the reaction rate, enhance homogeneity of species while, saving time and energy [22, 23].

As an important group of adsorbents, polymer matrix nanocomposites (PMNCs) consisting of organic (polymer matrix) and inorganic moieties (filler) have gained prominence among the other previous adsorbents [24, 25]. The outstandingly significant chemo-physical properties of PMNCs, such as relatively high external surface areas, high adsorption kinetics, chemically modifiable surface, low toxicity, and easy handling compared to powder-type adsorbents, have made them very desirable [24–27]. Nanostructured silica-based sorbents with porous structures have been studied and widely used for heavy metal ion removal. The last decade has seen mesoporous materials (MCMs, KITs, and SBAs) attract increasing attention due to their extraordinary properties such as porous structure, large surface areas, hydrophilic nature, good physicochemical resistance, and surface functional ability. MCM-41 (Mobil Composition of Matter No. 41) as a well-known mesoporous material has been utilized in numerous applications including catalysis, drug delivery, optical devices, adsorption, and extraction [26, 28–35]. In this paper, we report the synthesis and characterization of m-MCM-41/poly(methyl methacrylate) nanocomposites (m-MCM-41/PMMA NCs). The effectiveness of the synthesized nanocomposite for removal of Cu^{2+} ions from an aqueous solution has also been studied. The prepared NCs were characterized by Fourier transform

infrared spectroscopy (FT-IR), small angle x-ray scattering (SAXS), thermogravimetric analysis (TGA), transmission electron microscopy (TEM) and scanning electron microscopy (SEM) techniques. Different factors including pH, contact time, and initial Cu^{2+} concentrations were systematically investigated for metal ion adsorption. Modified Langmuir and Freundlich models were used for the evaluation of adsorption performance of copper ions while the adsorption kinetics parameters were likewise determined.

Experimental section

Materials

(3-Aminopropyl) trimethoxy silane ($\text{C}_9\text{H}_{23}\text{NO}_3\text{Si}$), methyl methacrylate (MMA, $\text{C}_5\text{H}_8\text{O}_2$), benzoyl peroxide (BP, $\text{C}_{14}\text{H}_{10}\text{O}_4$), copper(II) nitrate trihydrate ($\text{Cu}(\text{NO}_3)_2 \cdot 3\text{H}_2\text{O}$), HCl, NaOH, cetyltrimethylammonium bromide (CTAB, $[\text{C}_{16}\text{H}_{33}\text{N}(\text{CH}_3)_3]\text{Br}$), tetraethyl orthosilicate (TEOS, $\text{Si}(\text{OC}_2\text{H}_5)_4$), tetramethylammonium hydroxide (TMAOH, $\text{N}(\text{CH}_3)_4^+\text{OH}^-$), and toluene were purchased from Merck Chemical Co. Solvents (ethanol, toluene, and distilled water) were used as received.

Instrumentation

FT-IR analysis was acquired as KBr pellet by means of a Jasco FT/IR-680 plus spectrometer in the wavenumber range of $4000\text{--}400\text{ cm}^{-1}$ consist of 60 scans at a resolution of 4 cm^{-1} . The small angle X-ray scattering (SAXS) was measured by Bruker Nanostar-U by K_α radiation of Cu at $\lambda = 0.1542\text{ nm}$ at 100 mA and 45 kV. The scanning rate was $0.05^\circ\text{ min}^{-1}$ and X-ray scatterings were collected in the range of 2.0° and $3.5^\circ 2\theta$. TEM was performed using a CM120 electron microscope (Philips, Eindhoven, The Netherlands) worked at 120 kV. Images were obtained by means of a 2k CMOS TemCam F216 camera (camera and software, TVIPS, Munich, Germany). For SEM studies, a LEO 1530 (Zeiss, Oberkochen, Germany) were used. Thermogravimetric analyses (TGAs) were carried out from 20 to 800°C under inert atmosphere of argon and at $10^\circ\text{C min}^{-1}$ rate with a Netzsch STA-449F1. Flame atomic absorption spectroscopy (FAAS, PerkinElmer) was used for determination of Cu^{2+} concentrations in solution.

MCM-41 synthesis

MCM-41 was prepared based on the previously reported method [36]. This involved adding cetyltrimethylammonium bromide (5.22 g) and tetraethyl orthosilicate (TEOS) 10 wt% (30 mL) in tetramethylammonium hydroxide (12.25 mL) to water (47 mL) at room temperature to achieve

a supersaturated solution. The obtained solution was then stirred until the TEOS underwent full hydrolysis. After completion of the hydrolysis, a gel was obtained. The resulting gel was placed at 90 °C for 24 h in hydrothermal condition. The resultant precipitate was filtered, washed sufficiently, and dried. Calcination of the dried precipitate was performed at about 600 °C for 5 h.

m-MCM-41 synthesis

Surface functionalization of MCM-41 was performed *via* the following process. MCM-41 (0.4 g) was added to anhydrous ethanol (20 mL) and placed in an ultrasonic bath for 20 min at RT. Afterward, the silane coupling agent, 3-aminopropyl triethoxysilane, (0.2 mL) was added dropwise. Then it was stirred and refluxed at 90 °C overnight. The functionalized material was filtered, washed adequately with ethanol, and finally dried out at 60 °C.

m-MCM-41/PMMA nanocomposites synthesis by in situ polymerization

For the synthesis of the intended nanocomposites (4, 2, and 1 wt%) desired amounts of m-MCM-41 (0.100 g, 0.050 g, and 0.025 g) were added to three round bottom flasks containing 6 mL of anhydrous toluene, respectively. These were then placed in an ultrasonic bath for 45 min to obtain a colloidal dispersion of deagglomerated nanoparticles. This was followed by the addition of MMA (2.6 mL) under stirring. The reaction mixture was once again placed in the ultrasonic bath for 1 h. To initiate polymerization, BP (0.025 g) was added and the reaction mixtures kept under reflux and isothermal conditions for 6 h. Then it was again placed in the ultrasonic bath for 2 h. Finally, the mixtures were poured on a sheet of aluminum to get the NC films upon slow evaporation.

Adsorption experiments

Based on analysis data, 2 wt% NC was selected for adsorption studies. Batch mode was used for evaluation of adsorption experiments. The same adsorbent quantities (0.5 g L⁻¹) and copper(II) concentration (10 mg L⁻¹) were used for all experiments. Special polyethylene containers were used for shaking at 180 rpm and 25 °C for predetermined time intervals. Filtration of adsorbents over Whatman paper was done after attaining equilibrated adsorption conditions. FAAS was then used for measuring the remaining concentrations of Cu²⁺ ions in the filtrate. The experiments were repeated three times in the same condition and averaged.

Result and discussion

Characterization

The FT-IR spectra of the pristine filler (MCM-41), the modified ones (m-MCM-41), as well as 2 wt% NC (m-MCM-41/PMMA) are presented in Fig. 1. In the FT-IR spectrum of MCM-41 (Fig. 1a), several bands at 450 (Si–O–Si rocking), 802 (Si–O–Si bending), and 1075 cm⁻¹ (Si–O–Si stretching) emerged. The broad band at about 3500 cm⁻¹ is attributed to the O–H stretching mode of the surface silanols and adsorbed water molecules. For m-MCM-41, as depicted in Fig. 1b, the band at 457 cm⁻¹ is characteristic of Si–O–Si bending mode and the characteristics bands of aminopropyl groups were observed at 2925, 2855, and 1465 cm⁻¹, which were assigned as asymmetric C–H, symmetric C–H, and C–H bending mode of the silane coupling, respectively. The hydroxyl function of MCM-41 and amine groups of the silane coupling agent show up as a broad band in the 3500–3100 cm⁻¹ region (Fig. 1b). Figure 1c shows the

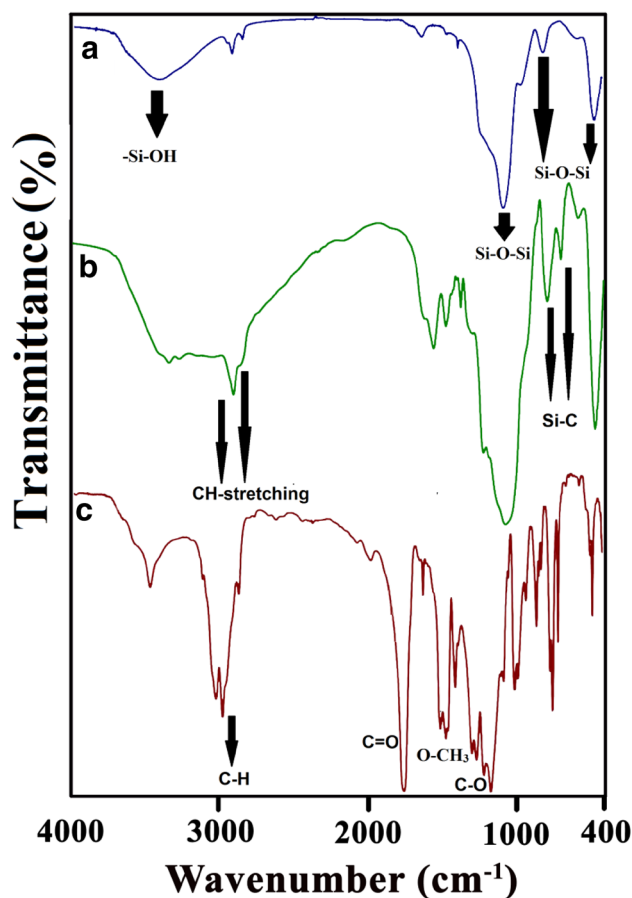


Fig. 1 FT-IR spectra of samples in the range of 4000–400 cm⁻¹ a MCM-41, b m-MCM-41, and c m-MCM-41/PMMA nanocomposite

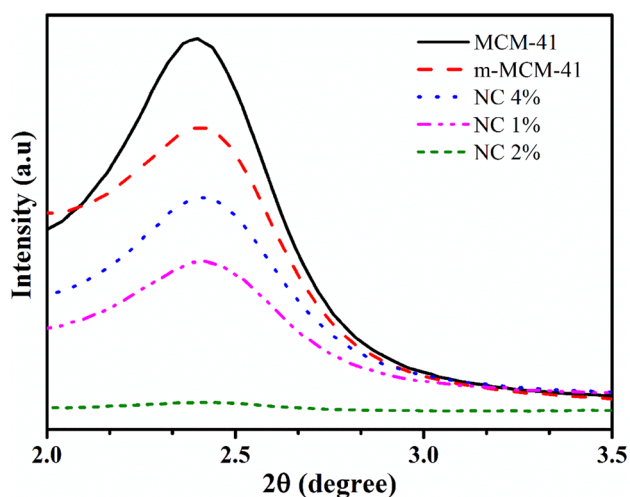


Fig. 2 SAXS diffractogram of pure and modified mesoporous filler as well as the NCs

FT-IR spectrum of m-MCM-41/PMMA NC. The appearance of a new absorption band at 1729 cm^{-1} is attributed to the vibration of the C=O ester group and 1242 cm^{-1} band shows the presence of C–O ester bond. The bands at 2997 cm^{-1} and 2951 cm^{-1} arise from the stretching vibration of the C–H bond. Two bands at 1450 and 1486 cm^{-1} are assigned to the bending vibrational mode of O–CH₃ and a strong peak at 1146 cm^{-1} originating from stretching mode of C–O bond.

The SAXS patterns of pure MCM-41, m-MCM-41 and m-MCM-41/PMMA NCs (1 wt%, 2 wt%, 4 wt%) are presented in Fig. 2. For m-MCM-41, the diffraction peak intensity decrement was observed after modifications, indicating that the pore structures were clearly affected by the modification. In the SAXS patterns of NCs, the intensities underwent decreases in this order: 4 wt% > 1 wt% > 2 wt%. One possible reason for the diminished intensity seen in 2 wt% NC could be low contrast for X-ray diffraction due to the presence of the voids as will be further confirmed from the SEM images (vide infra) [37].

Fig. 3 SEM images of m-MCM-41/PMMA NCs (1 wt%, 2 wt%, and 4 wt%)

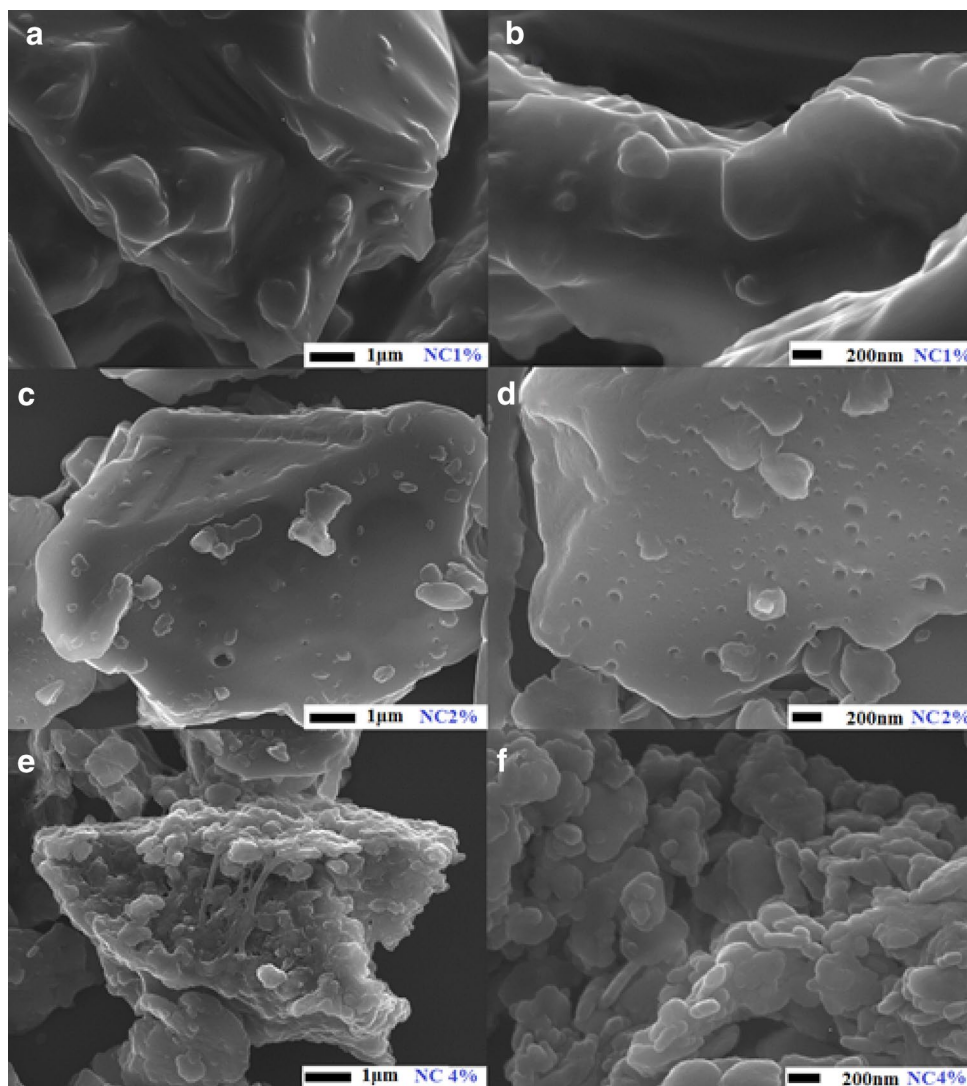


Fig. 4 TEM images of m-MCM-41/PMMA NCs 2 wt%

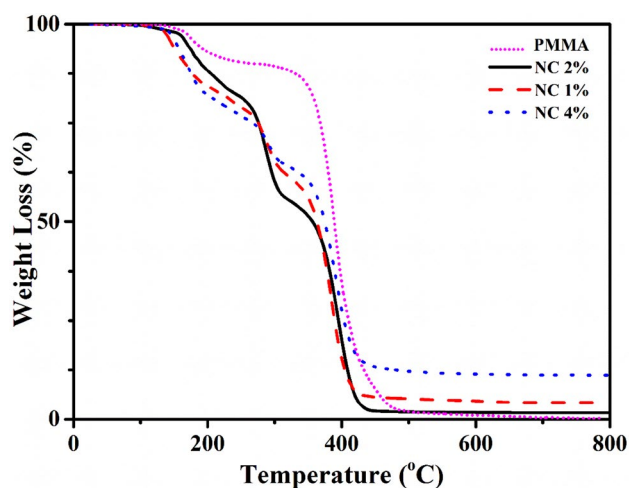
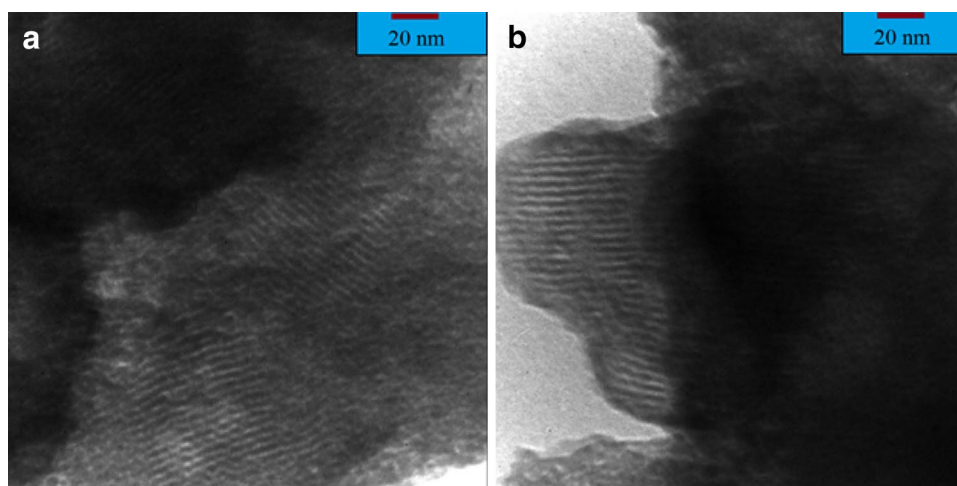


Fig. 5 TGA thermograms of PMMA and m-MCM-41/PMMA NCs (1 wt%, 2 wt%, and 4 wt%)

The surface morphology of m-MCM-41/PMMA NCs was evaluated by means of SEM techniques. As is evident from the SEM images, the ultrastructure of the samples is slightly different (Fig. 3). Where the 1 wt% NC shows mostly flat and soft surfaces, its 2 wt% analog shows more rough surfaces with nanopores, which is consistent with the unusual observed trends in the SAXS data. In the case of the 4 wt% NC, more cragged and granular surfaces were observed.

The porosity of the structure of the 2 wt% m-MCM-41/PMMA NC was evaluated using transmission electron microscopy (TEM) (Fig. 4). MCM-41 is porous silica with a regular hexagonal array of uniformly sized channels and it has been observed that the preparation method has no effect on its structure. The pore sizes of MCM-41 could be estimated to be 2–3 nm.

The thermal stabilities of the m-MCM-41/PMMA NCs (1 wt%, 2 wt%, and 4 wt%), and PMMA were examined using thermogravimetric analysis (TGA) as shown in Fig. 5.

Table 1 Thermal properties of the m-MCM-41/PMMA NCs (1 wt%, 2 wt%, and 4 wt%), and pure PMMA

Samples	$T_{5\%}$	$T_{10\%}$	LOI	Char yield
PMMA	183	267	17.6	0.2
NC 4 wt%	154	168	22.0	11.2
NC 2 wt%	169	190	18.1	1.6
NC 1 wt%	149	169	19.2	4.2

The thermal stability of NCs is higher than that of PMMA. Two separate and well-discrete weight-loss steps were observed in the TGA thermogram of the pristine polymer. The first weight-loss step occurs around 150 °C and ends about 280 °C, which would be due to the silane agents that are adsorbed on the surface of the m-MCM-41 or volatilization of residual adsorbed surface water. The next one begins at around 300 °C, and ends at about 500 °C, possibly stemming from the decomposition, elimination reactions of polymer, and self-combustion of organic constituents. TGA thermograms of the NCs showed three distinct and well-separated weight-loss steps. The first weight-loss step occurs at around 150–260 °C for all samples, which is assigned to the condensation of the surface hydroxyl or volatilization of physically absorbed the silane agent on the surface of the m-MCM 41. The next one begins at around 260 °C, and ends at about 330 °C, which is attributed to the decomposition of the silane coupling agent and the elimination reactions of the linear polymer. The last weight-loss stage starts at ca. 330 °C, and finishes at about 520 °C. TGA data related to the temperatures, for instance, T_x (temperature for x % weight loss), the amount of non-volatile material at 800 °C (char yield), and LOI (limiting oxygen index) are presented in Table 1.

LOI is the lowest concentration of oxygen in percentage, below which combustion of the polymer is not likely to proceed. A linear relationship exists between char yield

and LOI, which is expressed as the equation Van Krevelen and Hoftzyer (Eq. 1). If the LOI of a substance is more than atmospheric oxygen content (21%), it is considered as a fire-retardant material. While all the NCs showed high LOI values, only 4%wt NC showed an LOI of 22% (more than 21%). As it is shown in Table 1, the char yield was increased from 0.2% for PMMA to 11.2% for the 4%wt NC. These phenomena are a consequence of the increased nanoparticle-content and enhanced interaction with the polymer matrix, which leads to increased thermal stability. Interestingly, different thermal behaviors were observed for 2 wt% NC, as SAXS and SEM images have also shown, which would be a result of the porous structure of this NC that led to lower char yield. One possible explanation would be the higher air content in such nanopores for combustion and resultant lower char yield.

$$\text{LOI} = 17.5 + 0.4 \text{ Char yield.} \quad (1)$$

Adsorption

Concentration effect and isotherms

The adsorption of Cu^{2+} cations was evaluated by the investigation of Langmuir and Freundlich models as well as the modified Langmuir model [38]. The experiments were performed at 25 °C with an adsorbent dose of 0.01 g and pH value of 4 whilst the initial concentration of Cu^{2+} cations was varied in the range between 5.0 and 80.0 mg L^{-1} . The following equations are the linear expression of the Langmuir and Freundlich isotherm:

$$\frac{C_e}{q_e} = \frac{1}{K_L q_{\max}} + \frac{C_e}{q_{\max}}, \quad (2)$$

$$\log q_e = \log K_F + \frac{1}{n} \log C_e, \quad (3)$$

where in Eq. (2), C_e (mg L^{-1}) and q_e (mg g^{-1}) are the equilibrium concentration and adsorption capacity, respectively, q_{\max} (mg g^{-1}) and K_L are the maximum capacity and Langmuir constant, respectively. In the next equation (Eq. 3), K_F and n are the Freundlich isotherm constant indicating adsorption capacity and adsorption intensity, respectively. Equation (4) is the modified expression of the Langmuir isotherm where C_s (mg L^{-1}) is a saturated bulk solution

which is 2670 g L^{-1} for $\text{Cu}(\text{NO}_3)_2$ and K_{ML} is the modified Langmuir equilibrium constant [38]:

$$\frac{C_e}{q_e} = \frac{C_s}{K_{\text{ML}} q_{\max}} + \frac{(K_{\text{ML}} - 1)C_e}{K_{\text{ML}} q_{\max}}. \quad (4)$$

Data listed in Table 2 are the values of the maximum adsorption capacities (q_{\max}), Langmuir, modified Langmuir and Freundlich isotherm parameters derived from the equation of the line of the diagrams of Fig. 6. Langmuir and the modified Langmuir isotherm models show no differences and suggested to be well fitted with the experimental data of the NC due to its larger R^2 value.

The Freundlich isotherm demonstrates the adsorption process as a non-homogeneous multilayer process on the surface with an irregular distribution of adsorption heat because of the variety of adsorption positions over the heterogeneous surface. Moreover, the theoretical maximum adsorption capacity ($q_{\max, \text{cal}}$) of m-MCM-41/PMMA NC obtained using the Langmuir model and the experimental values ($q_{\max, \text{exp}}$) is reasonably close to each other. The $q_{\max, \text{cal}}$ of m-MCM-41/PMMA NC, which is calculated from the Langmuir model, is 40.95 mg g^{-1} .

pH effect

The adsorption capacity of the Cu^{2+} at different pH values (2–8) was studied under the following conditions: 10 mg L^{-1} of adsorbate, 0.5 g L^{-1} of adsorbent, 180 rpm, 298 K, and 240 min, the obtained results are presented in Fig. 7. As shown, the adsorption capacity underwent improvement as the pH increased from 2 to 4. Below this pH range, it is thought that the positive charges on the surface of the nanocomposites at pH values as well as the competition between hydrogen ions and Cu^{2+} led to a decrease in adsorption capacity. Between pH values 4–8, the adsorption quantity of Cu^{2+} also decreased and this is thought to be due to the increasing concentration of OH^- ions leading to the creation of anionic complexes of hydroxide. As a result, the concentration of the dissolved metal ions and their adsorption on the active sites would decrease. Accordingly, pH 4 was chosen as the optimum pH value for the adsorption of metal ions.

Table 2 Isotherm data for adsorption of Cu^{2+} ions on m-MCM-41/PMMA NC

m-MCM-41/PMMA NC	Langmuir			Modified Langmuir			Freundlich		
	q_{\max}	K_L (L mg^{-1})	R^2	q_{\max}	K_{ML}	R^2	K_F (mg g^{-1})	n	R^2
	40.95	0.2016	0.98809	40.95	538,277	0.98809	9.7724	2.44	0.9770

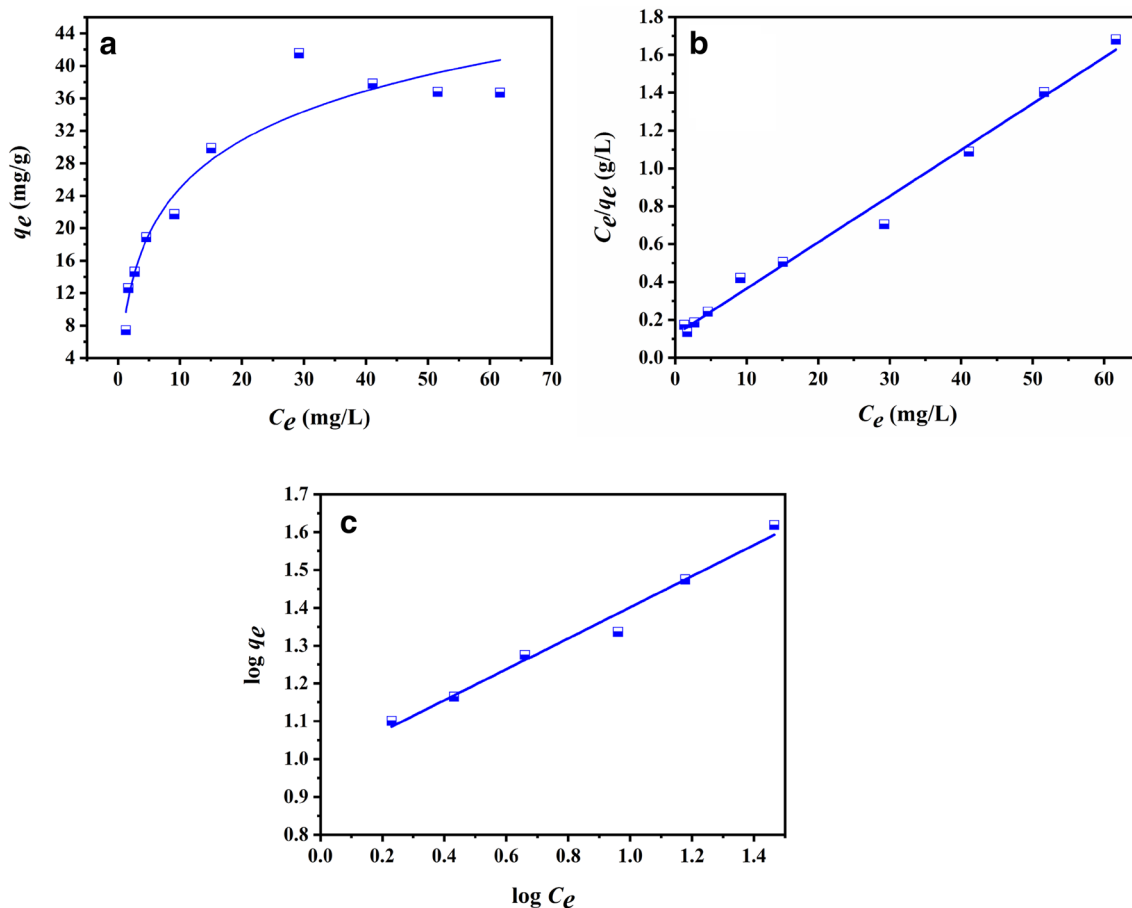


Fig. 6 The adsorption isotherm of Cu²⁺ ions **a** equilibrium isotherm, **b** Langmuir isotherm, and **c** Freundlich isotherm

Table 3 Kinetic parameters for the adsorption of Cu²⁺ ions

Kinetic models	Kinetic parameters	m-MCM-41/PMMA NC 2 wt%
Pseudo-second-order	k_{ad} (g mg ⁻¹ min ⁻¹)	2.07×10^{-3}
	q_e (mg g ⁻¹)	16.95
	α (mg g ⁻¹ min ⁻¹)	0.5945
	R^2	0.9891
Elovich	β (mg g ⁻¹ min ⁻¹)	0.3436
	R^2	0.8185
Intraparticle diffusion	k_{intra} (mg g ⁻¹ min ^{-1/2})	0.799
	C	4.826
	R^2	0.9166

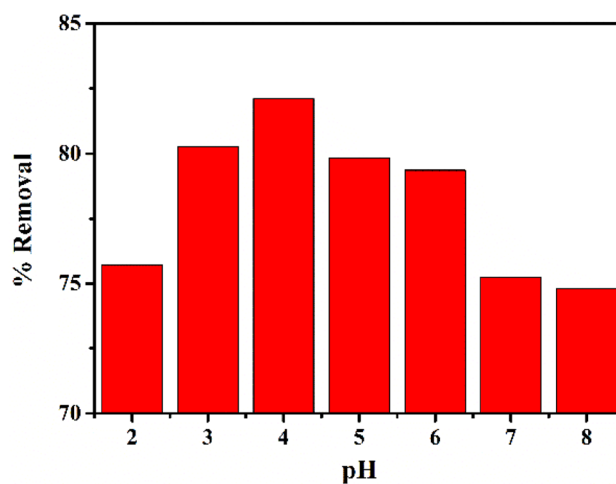


Fig. 7 Effect of pH on adsorption of Cu²⁺ ions

Contact time effect and kinetics of adsorption

The influence of contact time was undertaken on the adsorption of Cu^{2+} at the optimized pH value of 4. Figure 8a depicts the adsorption of Cu^{2+} ions on m-MCM-41/PMMA NC, which is fast and requires 140 min to reach to equilibrium. Consequently, the optimum contact time was selected to be 140 min.

The kinetics and mechanism of adsorption were studied via pseudo-second-order, Elovich, and intraparticle diffusion models. The following equations are representations of the pseudo-second-order model in its linear form:

$$\frac{t}{q_t} = -\frac{1}{\alpha} + \frac{t}{q_e} \quad (5)$$

$$\alpha = k_{\text{ad}} q_e^2 \quad (6)$$

The adsorption capacities, the value of adsorbed Cu^{2+} ions onto the adsorbent unit mass, are presented as q_e and q_t at equilibrium and at time t (mg g^{-1}), respectively.

The parameters α and k_{ad} are considered to be the initial adsorption rate ($\text{mg g}^{-1} \text{min}^{-1}$) and pseudo-second-order rate constant ($\text{g mg}^{-1} \text{min}^{-1}$), respectively. The corresponding diagrams are shown in Fig. 8b while the Elovich kinetic equation is shown in the following equation:

$$q_t = \frac{\ln(\alpha\beta)}{\beta} + \frac{\ln(t)}{\beta} \quad (7)$$

where the adsorption constant is represented by β ($\text{mg g}^{-1} \text{min}^{-1}$), and α and q_t are the same as mentioned earlier. Intraparticle diffusion kinetic is the possible method of species movement from solution into the solid phase and is described by the following equation:

$$q_t = k_{\text{intra}}(t)^{1/2} + C \quad (8)$$

The parameters C and k_{intra} are defined as rate constant and the intraparticle diffusion rate factor ($\text{mg g}^{-1} \text{min}^{-1/2}$), respectively. Intercepts and slopes of these plots including t/q_t and t , q_t and $\ln t$, and q_t and $t_{1/2}$ can be used for the calculation of the kinetic data of pseudo-second-order,

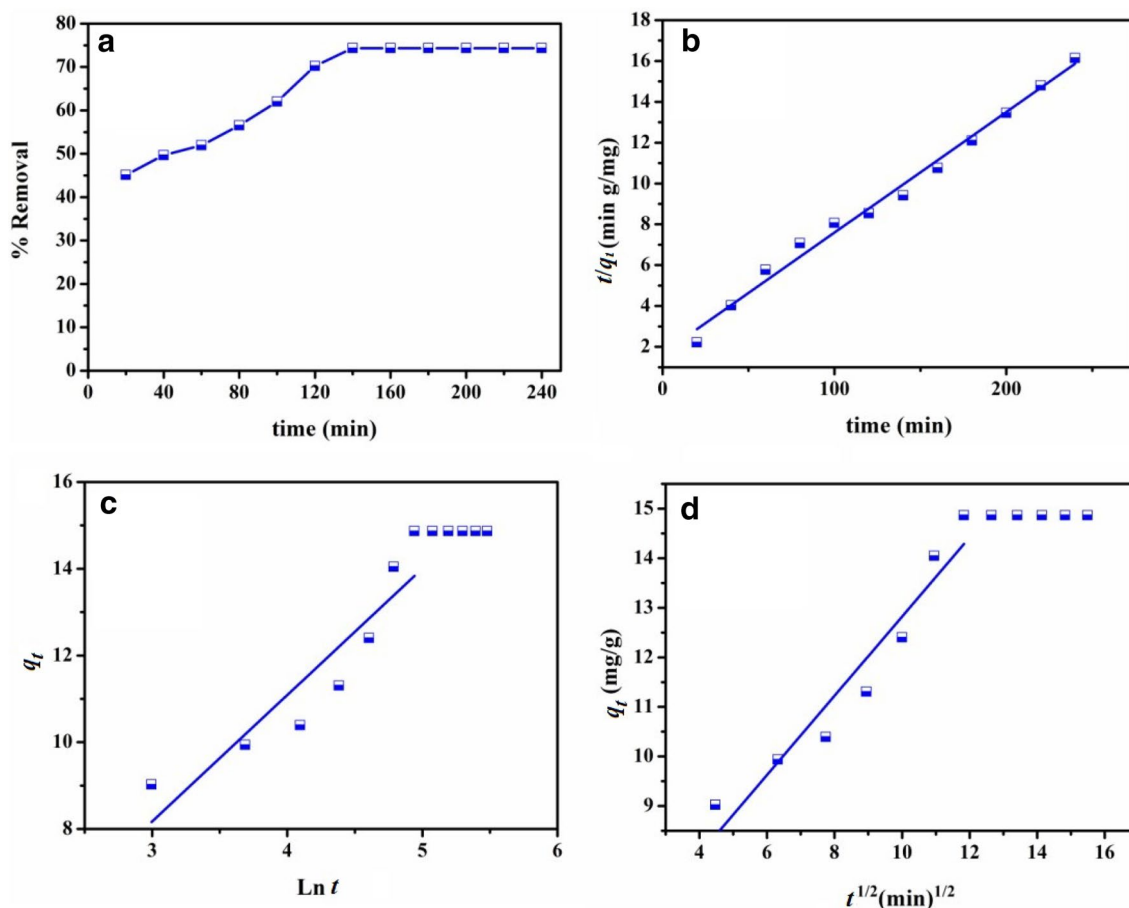


Fig. 8 a Contact time effect on Cu^{2+} adsorption, kinetic models for adsorption of Cu^{2+} ions, b pseudo-second-order, c Elovich, and d intraparticle diffusion models (20 mL of 10 mg L^{-1} Cu^{2+} solution, 10 mg of m-MCM-41/PMMA NC 2 wt%, 25°C , pH 4)

Table 4 Comparison of adsorption capacities toward Cu²⁺ ions

Adsorbents	Adsorption capacity (mg g ⁻¹)	References
Thiol-boehmite/PMMA 3 wt%	9.4	[27]
SBA-15	10.5	[39]
EDTA modified SBA-15	13.2	[40]
NH ₂ -SBA-15	19.2	[41]
NH ₂ -MCM-41	24.6	[42]
NH ₂ -MCM-41/nylon6	35.8	[43]
Thiol-SBA-16	36.4	[44]
Thiol-MCM-41	38.1	[45]
m-MCM-41/PMMA 2 wt%	41.5	This work
PVA/CC-ATS	45.4	[46]
Salicylaldehyde-SBA-15	59.0	[38]
KIT-6	76.9	[46]
Melamine-based NH ₂ -SBA-15	90.3	[40]
Thiol-KIT-6	102.0	[47]

Elovich, and intraparticle diffusion models, respectively (Fig. 8b–d).

The obtained data using all three kinetic models are summarized in Table 3. From this, it can be seen that the best R^2 value (correlation coefficient) for the adsorption of Cu²⁺ on m-MCM-41/PMMA NC is provided by the pseudo-second-order model. This is also consistent with provided theoretical data which found that at a lower initial concentration of the solute (here 10 mg L⁻¹) the kinetics model obeys pseudo-second-order [48, 49]. The superiority of this model over the other two, Elovich and intraparticle diffusion models, is a clear indication of the chemical nature of the adsorption process. Valence forces acting via electron-sharing/exchange between Cu²⁺ ions and a lone pair of electrons occurring in surface functional groups, such as C=O, OH, and NH₂ of m-MCM 41/PMMA NC are thought to be involved in the adsorption process. For comparison adsorption capacities (mg g⁻¹) of different adsorbents for Cu²⁺ removal are presented in Table 4.

Conclusions

m-MCM-41/PMMA was effectively synthesized by both in situ polymerization and ultrasonication method and used for adsorption of Cu²⁺ ions from aqueous solution. SEM, TEM, FT-IR, and TGA, as well as SAXS were utilized for a description of the prepared NCs. The analytical data revealed that among the three synthesized NCs, the 2 wt% NC has a different behavior as a result of its nanoporous morphology. Consequently, it was selected for Cu²⁺

adsorption experiments. The isothermal studies showed that equilibrium data fitted well with the Langmuir isotherm model. The adsorption capacity derived from Langmuir equation was 40.95 mg g⁻¹ at optimum pH = 4 and time (140 min) with 10 mg of adsorbent.

Acknowledgements This work was supported partially by the Research Affairs Division of Isfahan University of Technology (IUT).

References

1. G. Guo, F. Wu, F. Xie, R. Zhang, Spatial distribution and pollution assessment of heavy metals in urban soils from southwest China. *J. Environ. Sci.* **24**, 410–418 (2012)
2. M. Hua, S. Zhang, B. Pan, W. Zhang, L. Lv, Q. Zhang, Heavy metal removal from water/wastewater by nanosized metal oxides: a review. *J. Hazard. Mater.* **211**, 317–331 (2012)
3. F. Fu, Q. Wang, Removal of heavy metal ions from wastewaters: a review. *J. Environ. Manag.* **92**, 407–418 (2011)
4. M. Najafi, Y. Yousefi, A.A. Rafati, Synthesis, characterization and adsorption studies of several heavy metal ions on amino-functionalized silica nano hollow sphere and silica gel. *Sep. Purif. Technol.* **85**, 193–205 (2012)
5. H. Wang, C. Na, Binder-free carbon nanotube electrode for electrochemical removal of chromium. *ACS Appl. Mater. Interfaces* **6**, 20309–20316 (2014)
6. E. Eren, B. Afsin, Removal of basic dye using raw and acid activated bentonite samples. *J. Hazard. Mater.* **166**, 830–835 (2009)
7. A.T. Paulino, L.A. Belfiore, L.T. Kubota, E.C. Muniz, V.C. Almeida, E.B. Tambourgi, Effect of magnetite on the adsorption behavior of Pb(II), Cd(II), and Cu(II) in chitosan-based hydrogels. *Desalination* **275**, 187–196 (2011)
8. T. Phuengprasop, J. Sittiwong, F. Unob, Removal of heavy metal ions by iron oxide coated sewage sludge. *J. Hazard. Mater.* **186**, 502–507 (2011)
9. A.C. Balazs, T. Emrick, T.P. Russell, Nanoparticle polymer composites: where two small worlds meet. *Science* **314**, 1107–1110 (2006)
10. E. Lancelle-Beltran, P. Prené, C. Boscher, P. Belleville, P. Buvat, C. Sanchez, All-solid-state dye-sensitized nanoporous TiO₂ hybrid solar cells with high energy-conversion efficiency. *Adv. Mater.* **18**, 2579–2582 (2006)
11. C. Sanchez, B. Julián, P. Belleville, M. Popall, Applications of hybrid organic–inorganic nanocomposites. *J. Mater. Chem.* **15**, 3559–3592 (2005)
12. M.J. MacLachlan, I. Manners, G.A. Ozin, New(inter) faces: polymers and inorganic materials. *Adv. Mater.* **12**, 675–681 (2000)
13. G.A. Ozin, Nanochemistry: synthesis in diminishing dimensions. *Adv. Mater.* **4**, 612–649 (1992)
14. S.-C. Chang, J. Bharathan, Y. Yang, R. Helgeson, F. Wudl, M.B. Ramey, J.R. Reynolds, Dual-color polymer light-emitting pixels processed by hybrid inkjet printing. *Appl. Phys. Lett.* **73**, 2561–2563 (1998)
15. H. Siringhaus, T. Kawase, R. Friend, T. Shimoda, M. Inbasekaran, W. Wu, E. Woo, High-resolution inkjet printing of all-polymer transistor circuits. *Science* **290**, 2123–2126 (2000)
16. T. Kawase, T. Shimoda, C. Newsome, H. Siringhaus, R.H. Friend, Inkjet printing of polymer thin film transistors. *Thin Solid Films* **438**, 279–287 (2003)

17. Y. Xia, R.H. Friend, Controlled phase separation of polyfluorene blends via inkjet printing. *Macromolecules* **38**, 6466–6471 (2005)
18. J. Dijkman, P. Duineveld, M. Hack, A. Pierik, J. Rensen, J.-E. Rubingh, I. Schram, M. Vernhout, Precision ink jet printing of polymer light emitting displays. *J. Mater. Chem.* **17**, 511–522 (2007)
19. B.J. de Gans, P.C. Duineveld, U.S. Schubert, Inkjet printing of polymers: state of the art and future developments. *Adv. Mater.* **16**, 203–213 (2004)
20. E. Tekin, P.J. Smith, S. Hoepfener, A.M. van den Berg, A.S. Susha, A.L. Rogach, J. Feldmann, U.S. Schubert, Inkjet printing of luminescent CdTe nanocrystal–polymer composites. *Adv. Funct. Mater.* **17**, 23–28 (2007)
21. V. Marin, E. Holder, R. Hoogenboom, E. Tekin, U.S. Schubert, Light-emitting iridium (III) and ruthenium (II) polypyridyl complexes containing quadruple hydrogen-bonding moieties, *Dalton Trans.* **10**, 1636–1644 (2006)
22. M.A. Philip, U. Natarajan, R. Nagarajan, Acoustically-enhanced particle dispersion in polystyrene/alumina nanocomposites. *Adv. Nano Res.* **2**, 121–133 (2014)
23. P. Acar, Bozkurt, Sonochemical green synthesis of Ag/graphene nanocomposite. *Ultrason. Sonochem.* **35**, 397–404 (2017)
24. E.I. Unuabonah, A. Taubert, Clay–polymer nanocomposites (CPNs): adsorbents of the future for water treatment. *Appl. Clay Sci.* **99**, 83–92 (2014)
25. B. Samiey, C.-H. Cheng, J. Wu, Organic-inorganic hybrid polymers as adsorbents for removal of heavy metal ions from solutions: a review. *Materials* **7**, 673–726 (2014)
26. M. Dinari, G. Mohammadnezhad, R. Soltani, Fabrication of poly (methyl methacrylate)/silica KIT-6 nanocomposites via in situ polymerization approach and their application for removal of Cu²⁺ from aqueous solution. *RSC Adv.* **6**, 11419–11429 (2016)
27. G. Mohammadnezhad, M. Dinari, R. Soltani, The preparation of modified boehmite/PMMA nanocomposites by in situ polymerization and the assessment of their capability for Cu²⁺ ion removal. *New J. Chem.* **40**, 3612–3621 (2016)
28. F.-A. Zhang, D.-K. Lee, T.J. Pinnavaia, PMMA/mesoporous silica nanocomposites: effect of framework structure and pore size on thermomechanical properties. *Polym. Chem.* **1**, 107–113 (2010)
29. Z.A. AlOthman, A review: fundamental aspects of silicate mesoporous materials. *Materials* **5**, 2874–2902 (2012)
30. B. Naik, N.N. Ghosh, A review on chemical methodologies for preparation of mesoporous silica and alumina based materials. *Recent Patents Nanotechnol.* **3**, 213–224 (2009)
31. A. Heidari, H. Younesi, Z. Mehraban, Removal of Ni (II), Cd (II), and Pb (II) from a ternary aqueous solution by amino functionalized mesoporous and nano mesoporous silica. *Chem. Eng. J.* **153**, 70–79 (2009)
32. N. Vadia, S. Rajput, Mesoporous material, MCM-41: a new drug carrier. *Asian J. Pharm. Clin. Res.* **4**, 44–53 (2011)
33. X.S. Zhao, G. Lu, G.J. Millar, Advances in mesoporous molecular sieve MCM-41. *Ind. Eng. Chem. Res.* **35**, 2075–2090 (1996)
34. S. Mallakpour, E. Khadem, Facile and cost-effective preparation of PVA/modified calcium carbonate nanocomposites via ultrasonic irradiation: application in adsorption of heavy metal and oxygen permeation property. *Ultrason. Sonochem.* **39**, 430–438 (2017)
35. Issue, Information, *Polym. Compos.* **39**, 1–4 (2018)
36. M. Laghaei, M. Sadeghi, B. Ghalei, M. Dinari, The effect of various types of post-synthetic modifications on the structure and properties of MCM-41 mesoporous silica. *Prog. Org. Coat.* **90**, 163–170 (2016)
37. R. Liu, Y. Shi, Y. Wan, Y. Meng, F. Zhang, D. Gu, Z. Chen, B. Tu, D. Zhao, Triconstituent co-assembly to ordered mesostructured polymer–silica and carbon–silica nanocomposites and large-pore mesoporous carbons with high surface areas. *J. Am. Chem. Soc.* **128**, 11652–11662 (2006)
38. S. Azizian, S. Eris, L.D. Wilson, Re-evaluation of the century-old Langmuir isotherm for modeling adsorption phenomena in solution. *Chem. Phys.* **513**, 99–104 (2018)
39. M. Mureseanu, A. Reiss, I. Stefanescu, E. David, V. Parvulescu, G. Renard, V. Hulea, Modified SBA-15 mesoporous silica for heavy metal ions remediation. *Chemosphere* **73**, 1499–1504 (2008)
40. Y. Jiang, Q. Gao, H. Yu, Y. Chen, F. Deng, Intensively competitive adsorption for heavy metal ions by PAMAM-SBA-15 and EDTA-PAMAM-SBA-15 inorganic–organic hybrid materials. *Microporous Mesoporous Mater.* **103**, 316–324 (2007)
41. A. Shahbazi, H. Younesi, A. Badiei, Functionalized SBA-15 mesoporous silica by melamine-based dendrimer amines for adsorptive characteristics of Pb(II), Cu(II) and Cd(II) heavy metal ions in batch and fixed bed column. *Chem. Eng. J.* **168**, 505–518 (2011)
42. H. Yang, R. Xu, X. Xue, F. Li, G. Li, Hybrid surfactant-templated mesoporous silica formed in ethanol and its application for heavy metal removal. *J. Hazard. Mater.* **152**, 690–698 (2008)
43. G. Mohammadnezhad, R. Soltani, S. Abad, M. Dinari, A novel porous nanocomposite of aminated silica MCM-41 and nylon-6: isotherm, kinetic, and thermodynamic studies on adsorption of Cu(II) and Cd(II). *J. Appl. Polym. Sci.* **134**, 45383 (2017)
44. X. Xue, F. Li, Removal of Cu(II) from aqueous solution by adsorption onto functionalized SBA-16 mesoporous silica. *Microporous Mesoporous Mater.* **116**, 116–122 (2008)
45. S. Wu, F. Li, R. Xu, S. Wei, G. Li, Synthesis of thiol-functionalized MCM-41 mesoporous silicas and its application in Cu(II), Pb(II), Ag(I), and Cr(III) removal. *J. Nanopart. Res.* **12**, 2111–2124 (2010)
46. G. Mohammadnezhad, S. Abad, R. Soltani, M. Dinari, Study on thermal, mechanical and adsorption properties of amine-functionalized MCM-41/PMMA and MCM-41/PS nanocomposites prepared by ultrasonic irradiation. *Ultrason. Sonochem.* **39**, 765–773 (2017)
47. M. Dinari, G. Mohammadnezhad, R. Soltani, Fabrication of poly(methyl methacrylate)/silica KIT-6 nanocomposites via in situ polymerization approach and their application for removal of Cu²⁺ from aqueous solution. *RSC Adv.* **6**, 11419–11429 (2016)
48. Y. S. Ho, Review of second-order models for adsorption systems, *J. Hazard. Mater.* **136**(3), 681–689 (2006)
49. S. Azizian, Kinetic models of sorption: a theoretical analysis. *J. Colloid Interface Sci.* **276**(1), 47–52 (2004)